

SUPPORTING INFORMATION

for

Consistently high V_{oc} values in *p-i-n* type perovskite solar cells using Ni³⁺-doped NiO nanomesh as the hole transporting layer

Ujwal Kumar Thakur¹, Pawan Kumar¹, Sergey Gusarov², Alexander Kobryn², Saralyn Riddell¹, Ankur Goswami³, Kazi M. Alam¹, Spencer Savela¹, Piyush Kar¹, Thomas Thundat⁴, Alkiviathes Meldrum^{*5} and Karthik Shankar^{*1}

¹*Department of Electrical and Computer Engineering, University of Alberta, 9211-116 St, Edmonton, Alberta, T6G 1H9, Canada*

²*Nanotechnology Research Centre, National Research Council Canada, 11421 Saskatchewan Drive, Edmonton, Alberta, T6G 2M9, Canada*

³*Department of Materials Science and Engineering, Indian Institute of Technology, Hauz Khas, New Delhi, 11016, India*

⁴*Department of Chemical and Biological Engineering University at Buffalo, The State University of New York, NY 14260-4200, United States of America*

⁵*Department of Physics, University of Alberta, Edmonton, Alberta T6G 2E1, Canada*

*Email: Karthik Shankar (kshankar@ualberta.ca), Alkiviathes Meldrum (ameldrum@ualberta.ca)

1. Experimental Details:

1.1 Reagent and Materials

Analytical grade urea ($\geq 99\%$), chloroacetic acid ($\geq 99.0\%$), NiCl₂.6H₂O ($\geq 97.0\%$), formamidinium iodide (FAI) ($\geq 99\%$), PbI₂ (99%), methylammonium bromide (MABr) (98%) and PbBr₂ ($\geq 98\%$), PCBM (>99.5%) and procured from Sigma Aldrich and used as received without

any further purification. Sensiizer SQ2 was purchased from Solaronix and used without any purification. HPLC grade DMF, DMSO, chlorobenzene, isopropanol, and methanol were used in all the experiments without any further purification. Deionized water was used throughout experiments. Fluorine doped tin oxide (F: SnO₂, FTO) glass (transmittance 80-82%) was purchased from Hartford Tec Glass Company.

1.2 Structural and Physicochemical Characterization

The morphological features of thin films were investigated using Field emission scanning electron microscopy (FE-SEM) on a Zeiss Sigma FESEM operating at 5 kV an accelerating voltage. The fine morphological feature of NiO thin films was determined by using high-resolution transmission electron microscopy (HR-TEM), on a JEOL JEM-ARM200CF S/TEM equipped with EDX operating at an acceleration voltage of 200 kV. To see the film features, the sample was sliced by using a focused ion beam (FIB) having a Ga⁺ ion source. Before FIB operation the sample was coated with carbon and then a few nanometers of gold to protect film morphology and to reduce the charging effect. The obtained samples were analyzed under in HRTEM and acquired dm3 images were processed by using Gatan micrograph to calculate d spacing and diffraction planes.

The phase structure and crystalline properties of materials were determined by X-ray diffraction (XRD) pattern collected on a Bruker D8 Discover instrument using Cu-K α radiation (40 kV, $\lambda = 0.15418$ nm) equipped with a LynxEYE 1-dimensional detector. The spectra were collected in the range of 2 θ value 4–60° and step size was 0.02°.

Raman spectra to investigate specific vibrational feature of materials was recorded on a Thermo Scientific DXR2Raman Microscope using the 532 nm excitation line with an incident power of 20 mWcm⁻². The spectra were accumulated for 300 seconds using 50 μ m confocal pinhole apertures slit, a 2 cm⁻¹/CCD pixel element spectral dispersion grating. The sample was

deposited on a glass slide for the Raman measurement samples and laser spot was focused on the sample surface and the scattered light was collected.

X-ray photoelectron spectroscopy (XPS) for evaluating the surface chemical composition and oxidation state of NiO materials on FTO was acquired on XPS (Axis-Ultra, Kratos Analytical) instrument equipped with monochromatic Al-K α source (15 kV, 50 W) and photon energy of 1486.7 eV under ultrahigh vacuum ($\sim 10^{-8}$ Torr). The core level C1s XPS of adventitious carbon at BE \approx 284.8 eV was used as a standard for carbon correction to assign binding energy (BE) of other elements. CasaXPS software was used for processing of raw spectra and obtained deconvoluted spectra were plotted in Origin. Ultraviolet photoemission spectroscopy (UPS) was performed to determine work function and valence band spectra of samples were performed using a 21.21 eV He lamp as the excitation source.

To measure the optical band gap of NiO materials UV-Vis absorption spectra in diffuse reflectance mode was executed using a Perkin Elmer Lambda-1050 UV-Vis-NIR spectrophotometer equipped with an integrating sphere accessory. Photoluminescent behavior of the thin film was determined with steady-state photoluminescence (PL) spectra acquired on Varian Cary Eclipse fluorimeter xenon lamp excitation source and a slit width of 5 nm. Time-resolved photoluminescence (TRPL) lifetime decay curve to calculate the average lifetime of materials was recorded using a homemade single photon counting. A 405-nm picosecond diode laser (Alphalas GmbH) operated at a frequency of 13 MHz was used to excite the samples, and a Becker-Hickl HPM-100-50 PMT interfaced to an SPC-130 pulse counter system. The response time of setup was \sim 100 ps.

1.3 Surface area measurement of hole transport layers using the dye desorption technique

Freshly prepared compact and nanostructured NiO samples on FTO (1.5×2.5 cm) were treated with O₂ plasma for 5 min followed by overnight immersion in 1 mM SQ2 solution in methanol to form a monolayer of SQ2 dye over the available NiO surface. The obtained samples were rinsed with methanol and dried under nitrogen flow. For reference, a 7.8×10^{-6} M methanolic solution of SQ2 containing 0.1 M KOH was also prepared. The absorption spectrum of the reference sample is shown in Figure S8(a). The absorption spectra of nanostructured and compact NiO are presented in Figure S8(b) and (c), respectively (Supporting Information). The sharp absorption peak at ~ 656 nm in SQ2 coated nanostructured NiO and compact NiO validates the presence of SQ2 monolayer on the samples (Figure S8(d) and (e)). Subsequently, SQ2 was hydrolytically desorbed from the nanostructured and compact NiO samples using 3 mL of 0.1 M KOH dissolved in methanol. The absorption spectra of desorbed dye from nanostructured NiO and compact NiO samples were measured and used to calculate the coverage of dye on the surface. The area of one SQ2 molecule adsorbed on the surface was assumed to be $0.5 (\text{nm})^2$. The nanostructured NiO mesh electrode had a dye coverage of 3.8 nmol cm^{-2} while that of the NiO compact layer was 19.8 times lower.

References:

1. Dryza, V.; Bieske, E. J. Electron Injection and Energy-Transfer Properties of Spiropyran–Cyclodextrin Complexes Coated onto Metal Oxide Nanoparticles: Toward Photochromic Light Harvesting. *The Journal of Physical Chemistry C* 2015, 119, 14076-14084.
2. Godin, R.; Sherman, B. D.; Bergkamp, J. J.; Chesta, C. A.; Moore, A. L.; Moore, T. A.; Palacios, R. E.; Cosa, G. Charge-Transfer Dynamics of Fluorescent Dye-Sensitized Electrodes under Applied Biases. *The Journal of Physical Chemistry Letters* 2015, 6, 2688-269.

2. List of Figures and Tables:

Table S1: Photovoltaic performances of *p-i-n* type perovskite solar cells using undoped NiO and PEDOT:PSS as hole transporting layers.

Device Architecture	Photovoltaic Performance				Ref.
	V _{oc} (V)	J _{sc} (mA/cm ²)	FF	PCE (%)	
PEDOT:PSS as HTL					
ITO/PEDOT:PSS/SrGO/CH ₃ NH ₃ PbI ₃ /PCBM/BCP/Ag	1.04	19.39	0.80	16.01	1
ITO/PEDOT:PSS/CH ₃ NH ₃ PbI ₃ /PCBM/BCP/Ag	0.99	18.32	0.76	13.50	1
ITO/PEDOT:PSS/CH ₃ NH ₃ PbI ₃ /C ₆₀ /BCP/Al	0.87	17.70	0.72	11.09	2
ITO/PEDOT:PSS/PEG/CH ₃ NH ₃ PbI _x Cl _{1-x} /PCBM/Al	0.79	23.02	0.61	12.56	3
ITO/PEDOT:PSS/CH ₃ NH ₃ PbI ₃ /PCBM/Rhodamine/Ag	0.95	20.58	0.68	13.28	4
ITO/PEDOT:PSS/CH ₃ NH ₃ PbI ₃ /C ₆₀ /B4PyMPM/Ag	0.94	18.60	0.77	13.50	5
ITO/PEDOT:PSS/CH ₃ NH ₃ PbI ₃ .xtBP/PCBM/Al	0.97	20.47	0.80	15.90	6
ITO/QC-PEDOT:PSS/CH ₃ NH ₃ PbI ₃ .xtBP/PCBM/Al	1.02	21.13	0.82	17.67	6
ITO/PEDOT:PSS/CH ₃ NH ₃ PbI ₃ /PCBM/BCP/Ag	0.93	18.85	0.65	11.50	7
ITO/PEDOT:PSS(DMF)/CH ₃ NH ₃ PbI ₃ /PCBM/BCP/Ag	1.05	21.10	0.76	16.8	7
ITO/PEDOT:PSS/CH ₃ NH ₃ PbI _x Cl _{1-x} /PCBM/BCP/Ag	0.90	20.34	0.68	12.58	8
ITO/Ammonia-PEDOT:PSS/CH ₃ NH ₃ PbI _x Cl _{1-x} /PCBM/BCP/Ag	0.95	20.73	0.68	13.51	8
ITO/Ammonium phosphate-PEDOT:PSS/CH ₃ NH ₃ PbI _x Cl _{1-x} /PCBM/BCP/Ag	0.97	20.06	0.69	13.38	8
ITO/PEDOT:PSS/CH ₃ NH ₃ PbI _x Cl _{1-x} /PCBM/BCP/Ag	1.06	20.53	0.69	15.05	9
ITO/sodium citrate-PEDOT:PSS/CH ₃ NH ₃ PbI _x Cl _{1-x} /PCBM/BCP/Ag	1.13	21.62	0.75	18.39	9
ITO/PEDOT:PSS/CH ₃ NH ₃ PbI ₃ /PCBM/Rhodamine/LiF/Ag	1.00	20.62	0.80	16.57	10
ITO/CsI-PEDOT:PSS/CH ₃ NH ₃ PbI ₃ /PCBM/Rhodamine/LiF/Ag	1.08	22.58	0.83	20.22	10
ITO/PEDOT:PSS/CH ₃ NH ₃ PbI ₃ /PCBM/Ag	0.83	16.37	0.75	10.21	11
ITO/CTAB-PEDOT:PSS/CH ₃ NH ₃ PbI ₃ /PCBM/Rhodamine/LiF/Ag	0.90	18.62	0.75	12.53	11
ITO/PEDOT:PSS/CH ₃ NH ₃ PbI ₃ /PCBM/Ag	1.01	19.22	0.67	13.04	12
ITO/PEDOT:PSS/EA·HCl-CH ₃ NH ₃ PbI _x Cl _{1-x} /Bphen/Ag	0.92	22.85	0.80	16.97	13
ITO/PEDOT:PSS/MASCN-FAPb _{0.7} Sn _{0.3} I ₃ /PEAI/PCBM/BCP/Ag	0.78	26.46	0.79	16.26	14
ITO/PEDOT:PSS/FA _{0.6} MA _{0.4} Sn _{0.6} Pb _{0.4} I ₃ /PCBM/BCP/Ag	0.73	27.14	0.72	14.19	15
ITO/PFI-PEDOT:PSS/FA _{0.6} MA _{0.4} Sn _{0.6} Pb _{0.4} I ₃ /PCBM/BCP/Ag	0.78	27.22	0.74	15.85	15
ITO/PEDOT:PSS/CH ₃ NH ₃ PbI ₃ /C ₆₀ /BCP/Ag	0.90	17.36	0.71	11.12	16
ITO/PEDOT:PSS/TX-CH ₃ NH ₃ PbI ₃ /C ₆₀ /BCP/Ag	0.94	23.10	0.75	16.23	16
ITO/PEDOT:PSS/CH ₃ NH ₃ PbI _x Br _{3-x} /PCBM/ZnO/Ag	0.97	19.63	0.79	14.95	17
ITO/PEDOT:PSS:GO/CH ₃ NH ₃ PbI _x Br _{3-x} /PCBM/ZnO/Ag	1.02	21.55	0.82	18.09	17
ITO/PEDOT:PSS/CH ₃ NH ₃ PbI ₃ /PCBM/Bphen/Ag	0.96	16.56	0.78	12.40	18
ITO/PEPz-PEDOT:PSS/CH ₃ NH ₃ PbI ₃ /PCBM/Bphen/Ag	1.07	20.22	0.80	17.39	18
ITO/PEDOT:PSS/CH ₃ NH ₃ PbI _x Cl _{1-x} /PCBM/Ag	1.01	23.52	0.70	16.67	19
ITO/PEDOT:PSS/CH ₃ NH ₃ PbI ₃ /PCBM/BCP/Ag	1.05	22.40	0.73	17.26	20
ITO/PEDOT:PSS/CH ₃ NH ₃ PbI _x Cl _{1-x} /PCBM/Alq ₃ /Ag	1.01	19.56	0.72	14.22	21
NiO_x as HTL					
ITO/NiO _x /CH ₃ NH ₃ PbI ₃ /PCBM/BCP/Al	0.92	12.43	0.68	7.80	22
FTO/NiO/CH ₃ NH ₃ PbI ₃ /PCBM/BCP/Au	1.10	15.17	0.59	9.80	23
ITO/NiO/CH ₃ NH ₃ PbI ₃ /PCBM/Al	1.05	15.40	0.47	7.60	24
ITO/NiO _x /NiO _{nc} /CH ₃ NH ₃ PbI ₃ /PCBM/BCP/Al	0.96	19.80	0.61	11.60	25
ITO/NiO _x /NiO _{nc} /CH ₃ NH ₃ PbI ₃ /PCBM/BCP/Al	1.04	13.24	0.69	9.50	26

FTO/NiO _x / CH ₃ NH ₃ PbI ₃ /PCBM /Au	0.88	16.27	0.63	9.10	27
ITO/NiO/CH ₃ NH ₃ PbI ₃ /PCBM/LiF/Al	1.06	20.20	0.81	17.30	28
ITO/NiO _x /CH ₃ NH ₃ PbI ₃ /C ₆₀ /Ag	1.03	21.80	0.78	17.60	29
ITO/NiO/ Cs _{0.17} FA _{0.83} Pb(Br _{0.17} I _{0.83}) ₃ /LiF/PCBM/SnO ₂ /ZTO/ITO/LiF/Ag	0.98	18.70	0.79	14.50	30
ITO/NiO _x /CH ₃ NH ₃ PbI ₃ /PCBM /Ag	1.07	20.58	0.75	16.40	31
ITO/NiO/CH ₃ NH ₃ PbI ₃ /PCBM /Ag	1.04	21.87	0.72	16.40	32
ITO/NiO _x /CH ₃ NH ₃ PbI ₃ /ZnO /Al	1.01	21.00	0.76	16.10	33
FTO/NiO _x /CH ₃ NH ₃ PbI ₃ /PCBM /Ag	1.03	17.58	0.75	13.50	34
ITO/NiO _x /CH ₃ NH ₃ PbI _x Cl _{1-x} /PCBM/BCP/Ag	1.03	20.66	0.74	15.90	35
ITO/NiO _x /(FAPbI ₃) _{0.85} (MAPbBr ₃) _{0.15} /PCBM/ZnO/Ag	1.07	22.76	0.78	19.10	36
FTO/NiO/CH ₃ NH ₃ PbI ₃ (with additives)/PCBM/TiO ₂ /Ag	1.11	22.68	0.77	19.50	37
ITO/NiO/Cs _{0.05} (MA _{0.17} FA _{0.83}) _{0.95} Pb(I _{2.7} Br _{0.3})/PCBM/ZnO/Al	1.02	22.20	0.82	17.70	38
FTO/NiO/CH ₃ NH ₃ PbI ₃ /PCBM/BCP/Au	1.06	19.41	0.75	15.40	39
FTO/NiO/CH ₃ NH ₃ PbI ₃ /PCBM/BCP/Ag	1.05	20.57	0.75	16.20	34
FTO/NiO _x / MA _{1-y} FA _y PbI _{3-x} Cl _x /PCBM/BCP/Ag	1.12	23.70	0.76	20.20	40
ITO/NiO _x /CH ₃ NH ₃ PbI ₃ /C ₆₀ /BCP/Al	0.99	19.84	0.75	14.61	2
FTO/NiO _x / CH ₃ NH ₃ PbI ₃ /PCBM/Ag	1.10	21.90	0.72	17.30	41

Table S2: Calculated HOMO and LUMO energies for perovskites particles and their energies of adsorption on NiO surface for two different geometries G2 and G3.

	HOMO, eV	LUMO, eV	E_{ads} , G2, eV	E_{ads} , G3, eV
$\text{CH}_3\text{NH}_3\text{PbBr}_3$	-5.60	-3.99	6.12	9.75
$\text{CH}_3\text{NH}_3\text{PbI}_3$	-5.59	-4.08	4.13	8.01

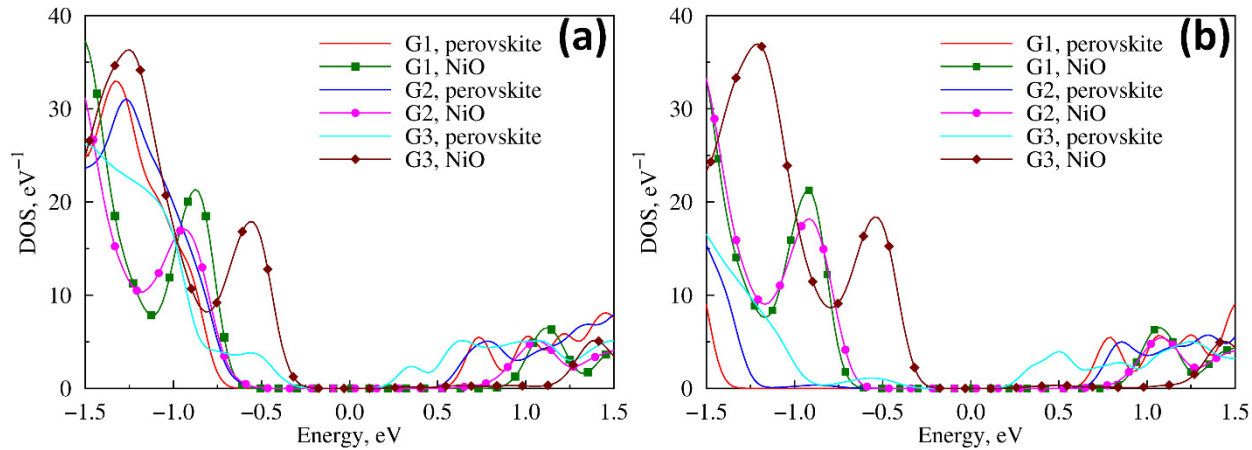


Figure S1: Density of state distribution for NiO surface and (a) MAPbI_3 cluster and (b) MAPbBr_3 cluster.

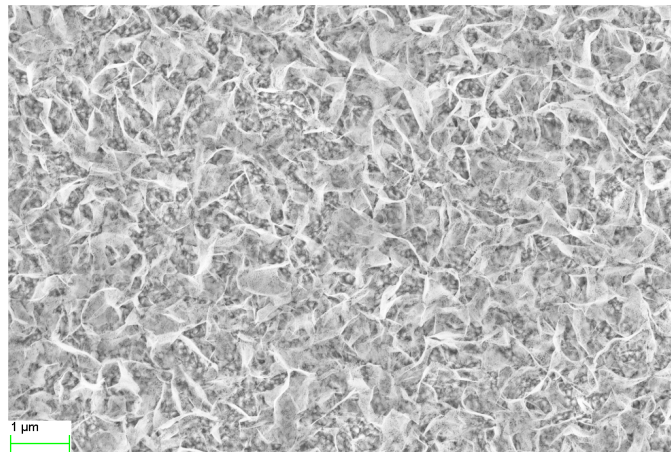


Figure S2: Top SEM image of NiO nanostructure made with 0.5 mM concentration of $\text{NiCl}_2 \cdot 6\text{H}_2\text{O}$ in growth solution showing exposed FTO substrate.

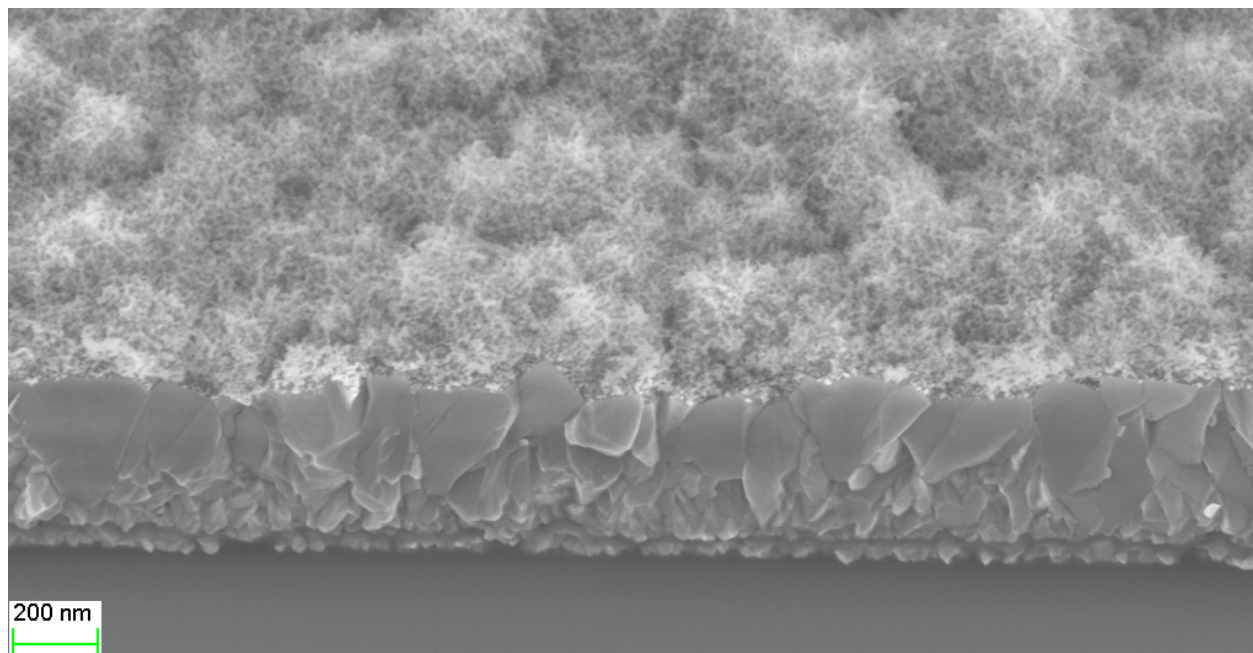


Figure S3: Tilted cross-sectional SEM image of NiO nanostructure made with a 1.0 mM concentration of $\text{NiCl}_2 \cdot 6\text{H}_2\text{O}$ in growth solution shows conformal deposition of NiO on FTO substrate.

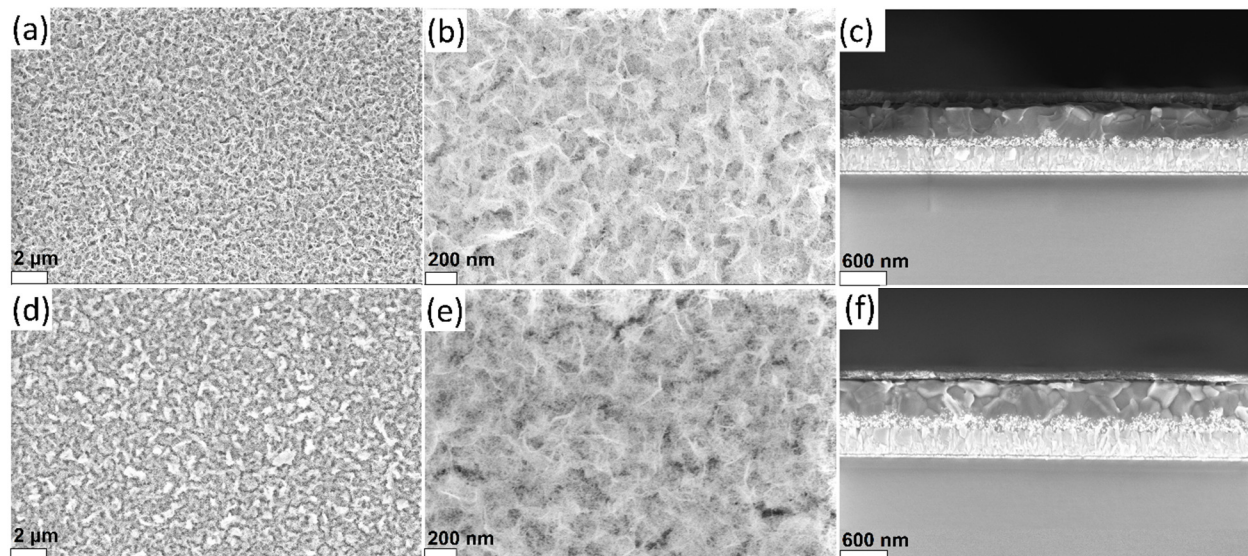


Figure S4: Top-view FESEM images of NiO nanostructure (a, b) made with 3 mM and (d,e) 5 mM of $\text{NiCl}_2 \cdot 6\text{H}_2\text{O}$. Cross-sectional image of perovskite solar cell made with (c) 3 mM and (f) 5 mM of $\text{NiCl}_2 \cdot 6\text{H}_2\text{O}$.

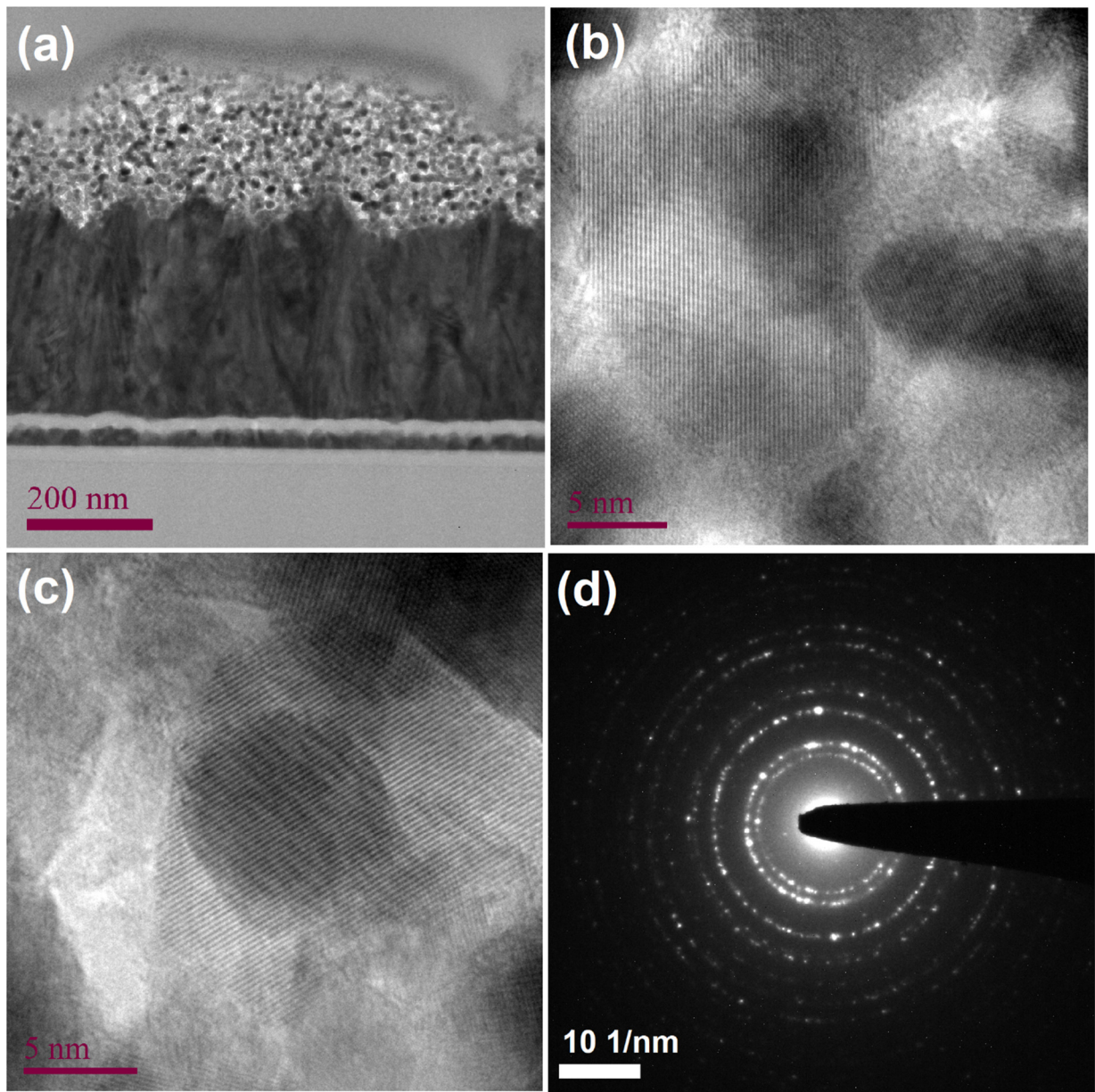


Figure S5: HR-TEM image of nanostructure NiO film (1 mM $\text{NiCl}_2 \cdot 6\text{H}_2\text{O}$) (a) side view of FIB snipped sample, (b) and (c) high magnification TEM images at 5 nm scale bar showing lattice fringes, and (d) SAED pattern showing diffraction rings.

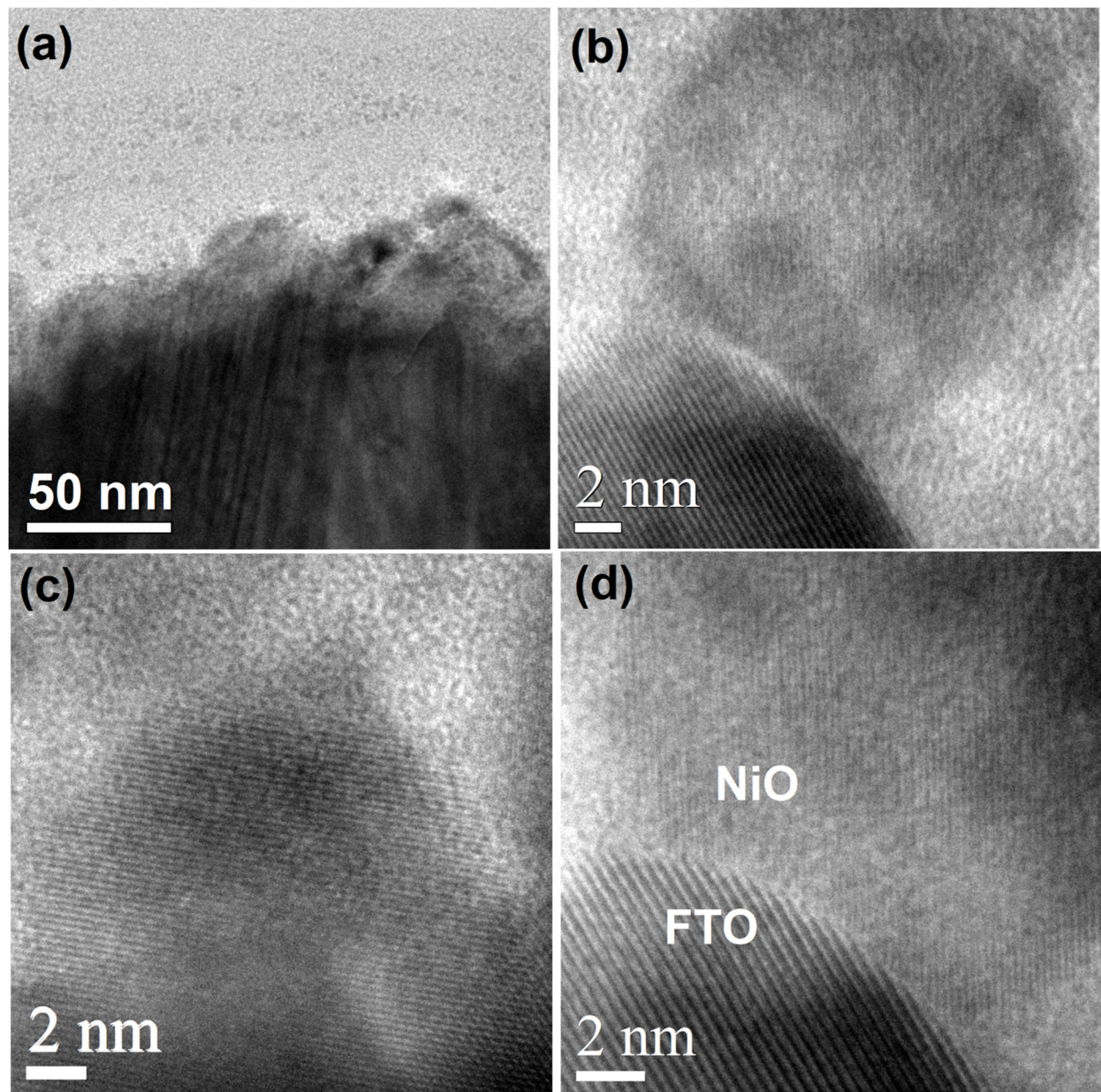


Figure S6: HR-TEM image of compact NiO thin film (a) side view of FIB snipped sample, (b) and (c) high magnification TEM images at 5 nm scale bar and (d) TEM image showing FTO and NiO interfacial contact.

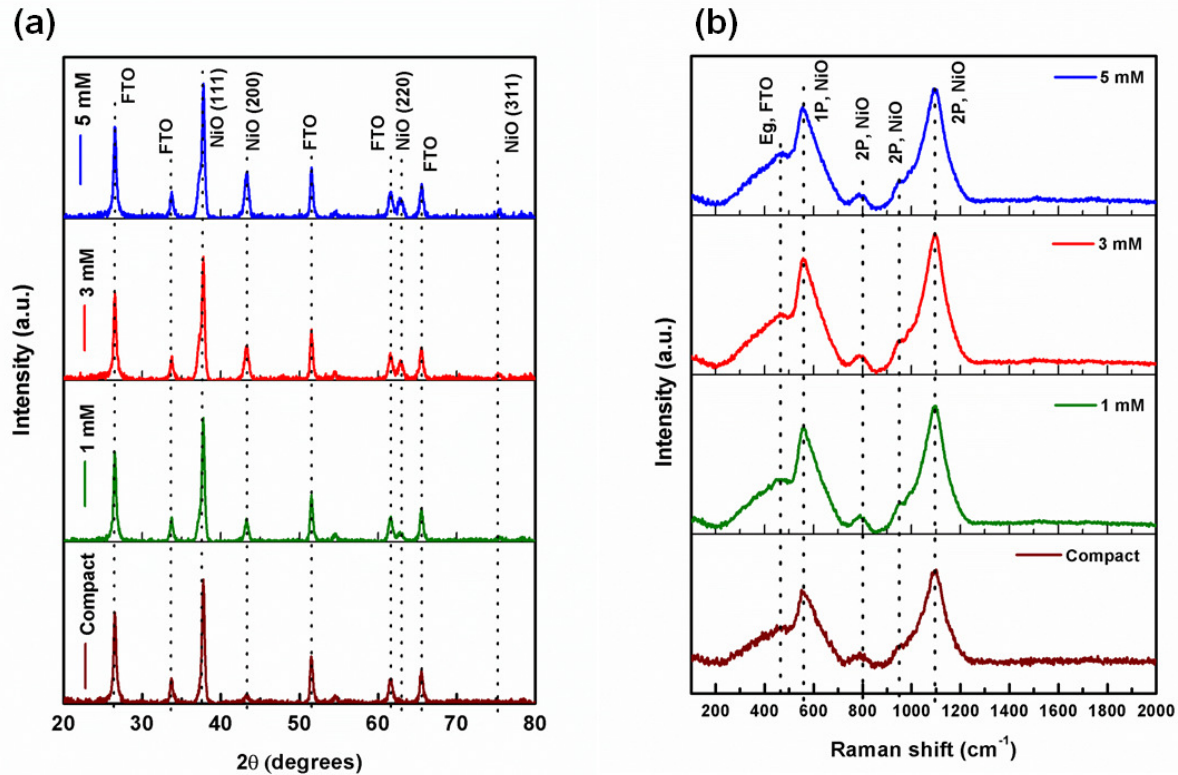


Figure S7: (a) XRD spectra and (b) Raman spectra of compact NiO and NiO nanostructures prepared with different concentration of $\text{NiCl}_2 \cdot 6\text{H}_2\text{O}$ in hydrothermal growth solution.

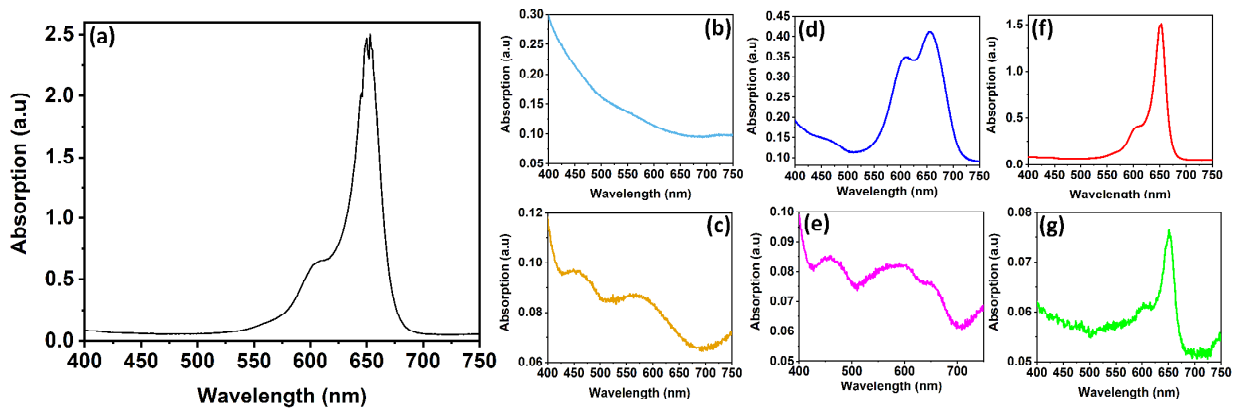


Figure S8: UV-vis absorption spectra of (a) SQ2 dissolved in 0.1 M KOH, (b), FTO deposited nanostructured NiO and (c) compact NiO, monolayer SQ2 deposited over (d) nanostructured NiO and (e) compact NiO, KOH assisted desorbed SQ2 from (f) nanostructured and (g) compact NiO.

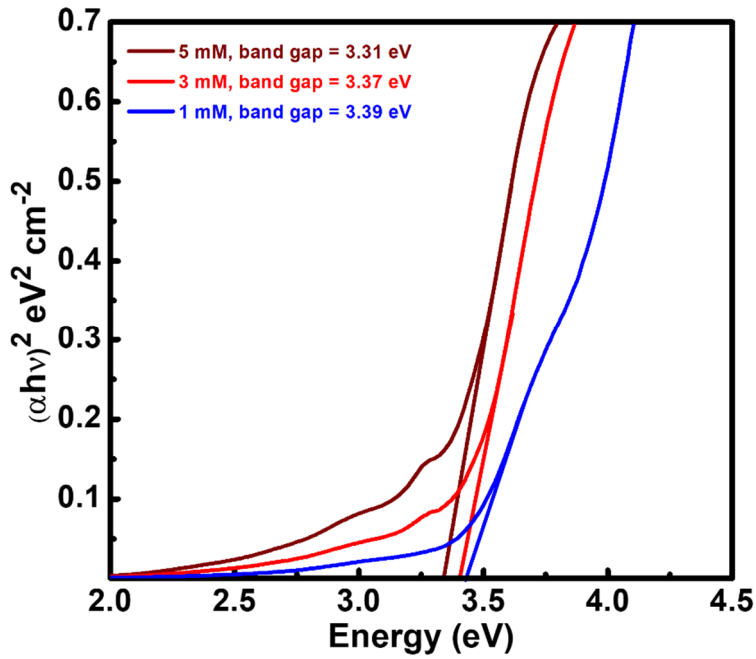


Figure S9: Tauc plots of NiO nanostructures made with different concentration of $\text{NiCl}_2 \cdot 6\text{H}_2\text{O}$ in growth solution.

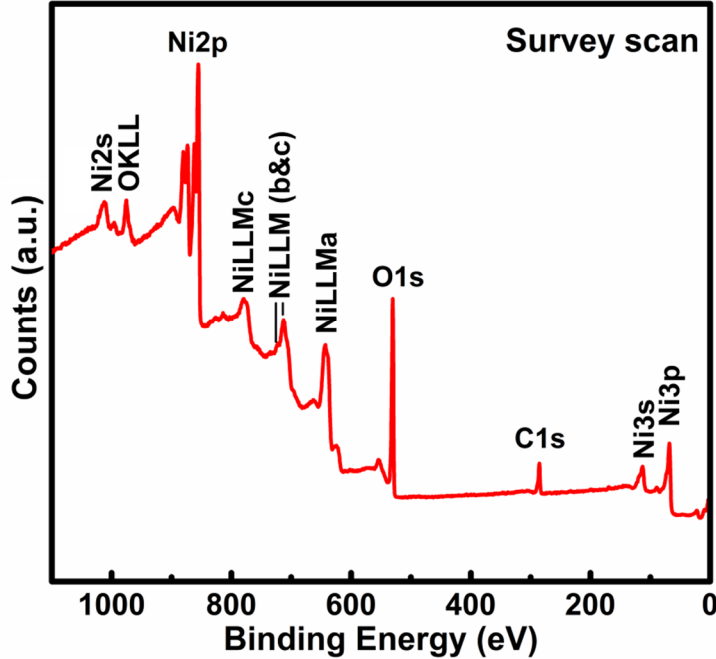


Figure S10: XPS elemental survey scan of NiO network thin film.

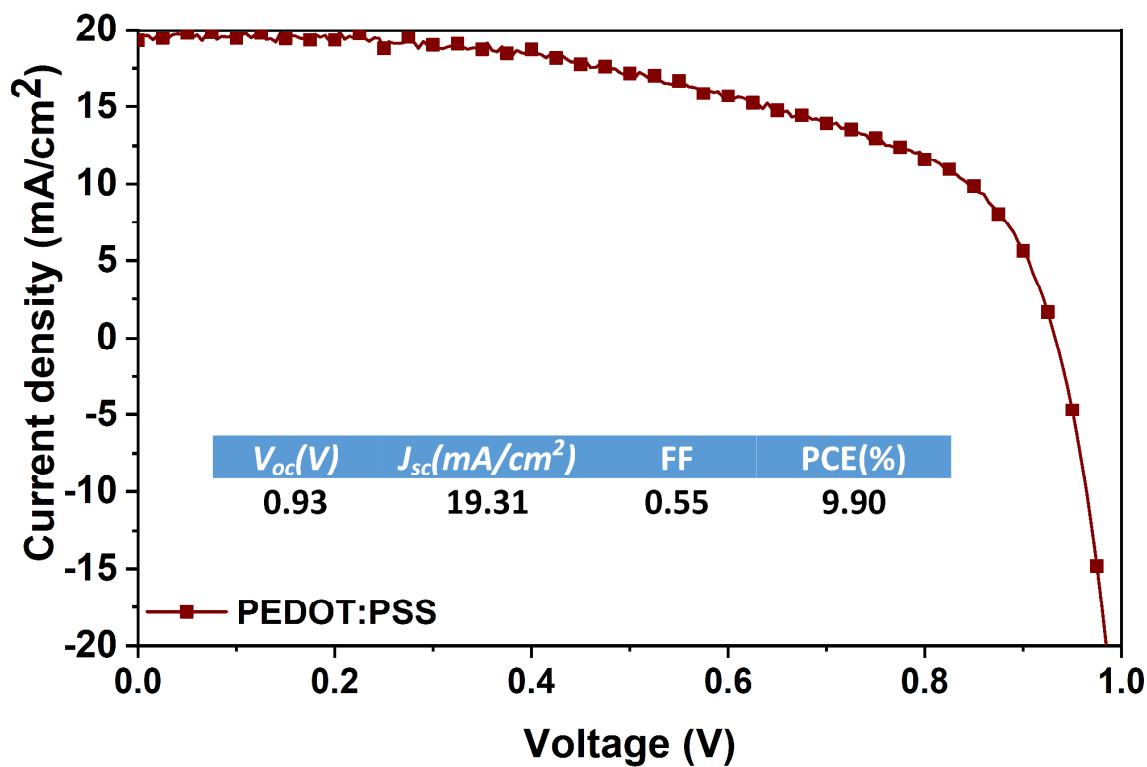


Figure S11: Current-voltage curves of perovskite solar cell made with PEDOT: PSS as hole transporting layer. The measurement was carried out under AM1.5 G illumination at 100 mW/cm^2 with an active area of 6 mm^2 .

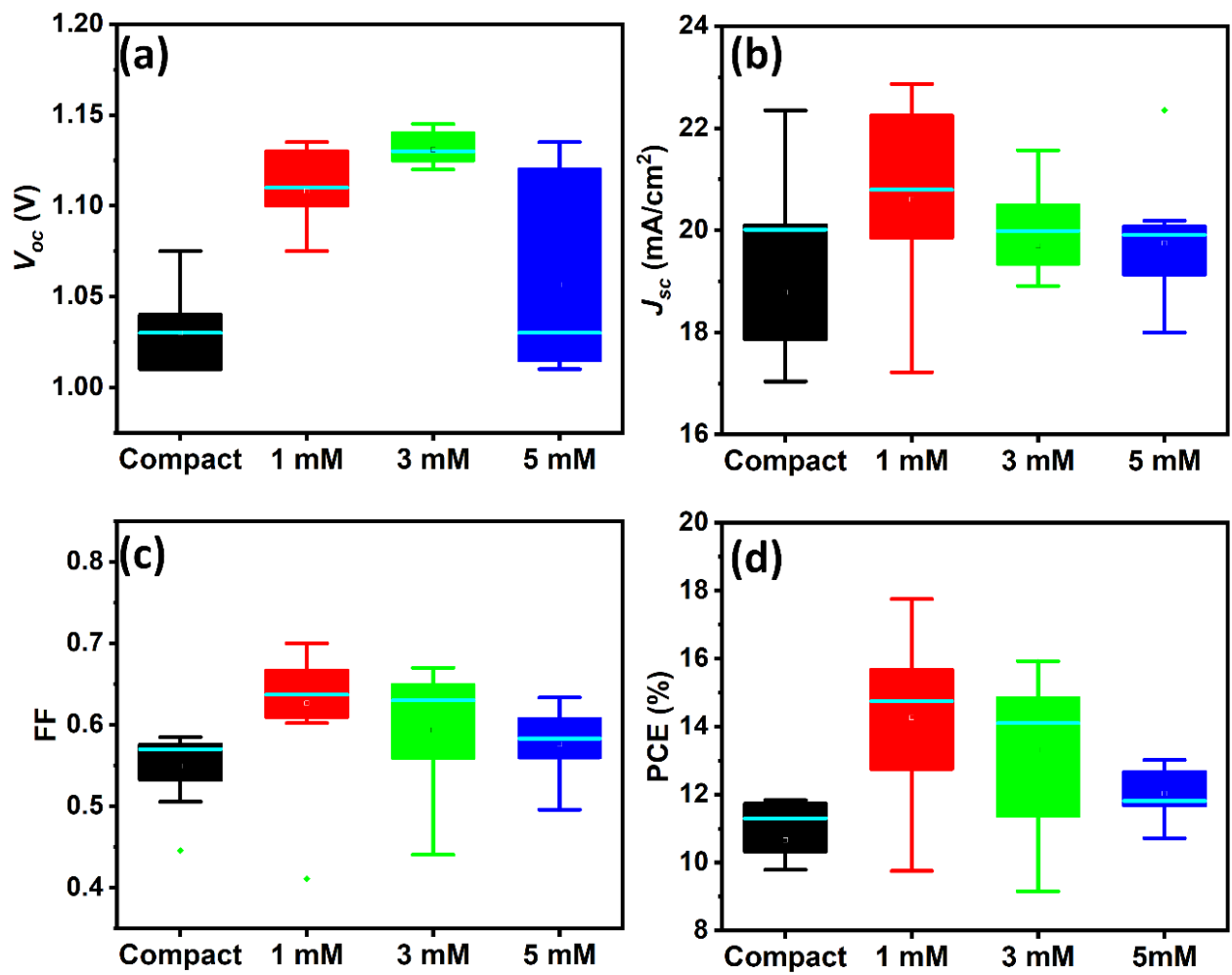


Figure S12: Box charts of (a) V_{oc} , (b) J_{sc} , (c) FF and (d) PCE for perovskite solar cells based on compact NiO and NiO nanostructure made with different concentration of NiCl₂.6H₂O.

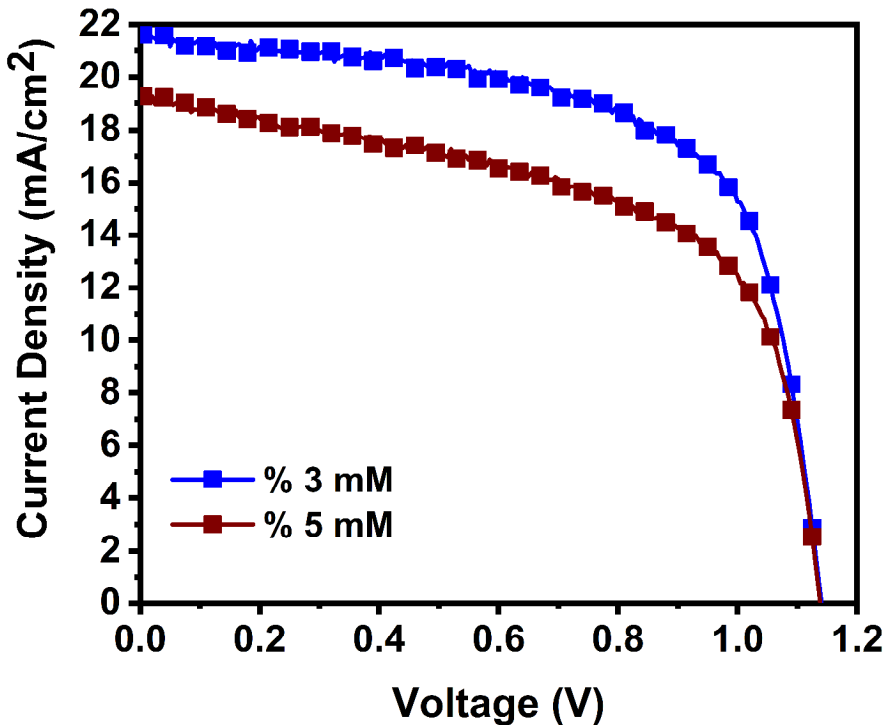


Figure S13: Current-voltage curves of perovskite solar cell made with nanostructure NiO hole transporting layer made with 3 mM and 5 mM of NiCl₂·6H₂O. The measurement was carried out under AM1.5 G illumination at 100 mW/cm² with an active area of 6 mm².

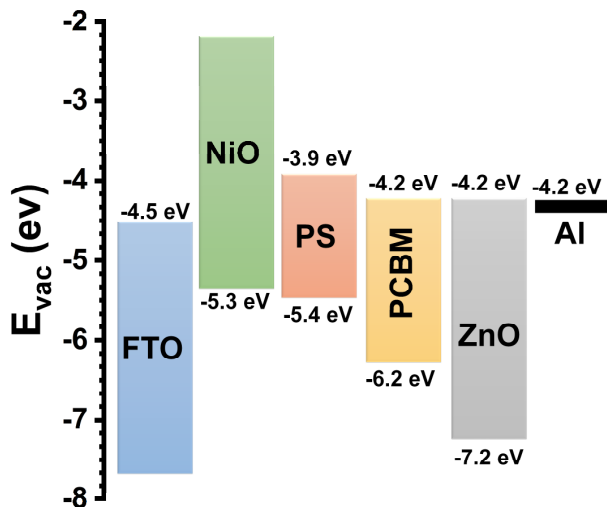


Figure S14: Energy band diagram for an inverted perovskite solar cell with the structure of FTO/NiO nanostructure/perovskite absorber layer/PCBM/ZnO/Al.

Table S3: Fitting parameters of time resolved photoluminescence spectra for HTL free perovskite layer and perovskite layer deposited over compact and nanostructured NiO coated FTO substrate. The values of the goodness-of-fit parameter (r^2) are all close to 1.0.

	A_1	τ_1	A_2	τ_2	A_3	τ_3	τ_{avg}
Bare FTO	0.43	11.92	0.39	151.37	-	-	54.73
FTO/Compact NiO	0.89	1.71	0.13	13.19	0.041	569.89	20.17
FTO/NiO nanostructure	0.85	1.55	0.19	8.37	0.013	122.25	1.51

3. References:

1. Mann, D. S.; Seo, Y.-H.; Kwon, S.-N.; Na, S.-I. Efficient and Stable Planar Perovskite Solar Cells With a PEDOT:PSS/SrGO Hole Interfacial Layer. *J. Alloys Compd.* **2020**, 812, 152091.
2. Wu, P.-T.; Tsai, M.-C.; Guo, T.-F.; Fu, Y.-S. The Impact at Polar Solvent Treatment on p-Contact Layers (PEDOT:PSS or NiO_x) of Hybrid Perovskite Solar Cells. *Org. Electron.* **2019**, 73, 273-278.
3. Zhang, R.; Ling, H.; Lu, X.; Xia, J. The Facile Modification of PEDOT:PSS Buffer Layer by Polyethyleneglycol and Their Effects on Inverted Perovskite Solar Cell. *Solar Energy* **2019**, 186, 398-403.
4. Reza, K. M.; Gurung, A.; Bahrami, B.; Mabrouk, S.; Elbohy, H.; Pathak, R.; Chen, K.; Chowdhury, A. H.; Rahman, M. T.; Letourneau, S.; Yang, H.-C.; Saianand, G.; Elam, J. W.; Darling, S. B.; Qiao, Q. Tailored PEDOT:PSS Hole Transport Layer for Higher Performance in Perovskite Solar cells: Enhancement of Electrical and Optical Properties with Improved Morphology. *J. Energy Chem.* **2020**, 44, 41-50.
5. Yang, D.; Sano, T.; Yaguchi, Y.; Sun, H.; Sasabe, H.; Kido, J. Achieving 20% Efficiency for Low-Temperature-Processed Inverted Perovskite Solar Cells. *Adv. Funct. Mater.* **2019**, 29, 1807556.
6. Chen, W.-H.; Qiu, L.; Zhang, P.; Jiang, P.-C.; Du, P.; Song, L.; Xiong, J.; Ko, F. Simple Fabrication of a Highly Conductive and Passivated PEDOT:PSS Film via Cryo-Controlled Quasi-Congealing Spin-Coating for Flexible Perovskite Solar Cells. *J. Mater. Chem. C* **2019**, 7, 10247-10256.
7. Li, H.; Zhang, C.; Ma, Y.; Li, Z.; Xu, Y.; Mai, Y. Homogenizing the Sulfonic Acid Distribution of DMF-Modified PEDOT:PSS Films and Perovskite Solar Cells. *J. Energy Chem.* **2019**, 32, 71-77.
8. Wang, Y.; Hu, Y.; Han, D.; Yuan, Q.; Cao, T.; Chen, N.; Zhou, D.; Cong, H.; Feng, L. Ammonia-Treated Graphene Oxide and PEDOT:PSS as Hole Transport Layer for High-Performance Perovskite Solar Cells with Enhanced Stability. *Org. Electron.* **2019**, 70, 63-70.
9. Hu, W.; Xu, C. Y.; Niu, L. B.; Elseman, A. M.; Wang, G.; Liu, D. B.; Yao, Y. Q.; Liao, L. P.; Zhou, G. D.; Song, Q. L. High Open-Circuit Voltage of 1.134 V for Inverted Planar Perovskite Solar Cells with Sodium Citrate-Doped PEDOT:PSS as a Hole Transport Layer. *ACS Appl. Mater. Inter.* **2019**, 11, 22021-22027.
10. Jiang, K.; Wu, F.; Zhang, G.; Chow, P. C. Y.; Ma, C.; Li, S.; Wong, K. S.; Zhu, L.; Yan, H. Inverted Planar Perovskite Solar Cells Based on CsI-doped PEDOT:PSS with Efficiency Beyond 20% and Small Energy Loss. *J. Mater. Chem. A* **2019**, 7, 21662-21667.
11. Zhu, Y.; Wang, S.; Ma, R.; Wang, C. The improvement of Inverted Perovskite Solar Cells by the Introduction of CTAB into PEDOT:PSS. *Solar Energy* **2019**, 188, 28-34.
12. Yalcin, E.; Can, M.; Rodriguez-Seco, C.; Aktas, E.; Pudi, R.; Cambarau, W.; Demic, S.; Palomares, E. Semiconductor Self-Assembled Monolayers as Selective Contacts for Efficient PiN Perovskite Solar Cells. *Energ. Environ. Sci.* **2019**, 12, 230-237.

13. Zhu, K.; Cong, S.; Lu, Z.; Lou, Y.; He, L.; Li, J.; Ding, J.; Yuang, N.; Rümmeli, M. H.; Zou, G. Enhanced Perovskite Solar Cell Performance via Defect Passivation with Ethylamine Alcohol Chlorides Additive. *J. Power Sources* **2019**, *428*, 82-87.
14. Lian, X.; Chen, J.; Zhang, Y.; Qin, M.; Li, J.; Tian, S.; Yang, W.; Lu, X.; Wu, G.; Chen, H. Highly Efficient Sn/Pb Binary Perovskite Solar Cell via Precursor Engineering: A Two-Step Fabrication Process. **2019**, *29*, 1807024.
15. Tang, H.; Shang, Y.; Zhou, W.; Peng, Z.; Ning, Z. Energy Level Tuning of PEDOT:PSS for High Performance Tin-Lead Mixed Perovskite Solar Cells. *Solar RRL* **2019**, *3*, 1800256.
16. Shin, D.; Kang, D.; Lee, J.-B.; Ahn, J.-H.; Cho, I.-W.; Ryu, M.-Y.; Cho, S. W.; Jung, N. E.; Lee, H.; Yi, Y. Electronic Structure of Nonionic Surfactant-Modified PEDOT:PSS and Its Application in Perovskite Solar Cells with Reduced Interface Recombination. *ACS Appl. Mater. Inter.* **2019**, *11*, 17028-17034.
17. Yu, J. C.; Hong, J. A.; Jung, E. D.; Kim, D. B.; Baek, S.-M.; Lee, S.; Cho, S.; Park, S. S.; Choi, K. J.; Song, M. H. Highly Efficient and Stable Inverted Perovskite Solar Cell Employing PEDOT:GO Composite Layer as a Hole Transport Layer. *Sci. Rep.* **2018**, *8*, 1070.
18. Huang, D.; Goh, T.; McMillon-Brown, L.; Kong, J.; Zheng, Y.; Zhao, J.; Li, Y.; Zhao, S.; Xu, Z.; Taylor, A. D. PEOz-PEDOT:PSS Composite Layer: A Route to Suppressed Hysteresis and Enhanced Open-Circuit Voltage in a Planar Perovskite Solar Cell. *ACS Appl. Mater. Inter.* **2018**, *10*, 25329-25336.
19. Wang, M.; Zang, Z.; Yang, B.; Hu, X.; Sun, K.; Sun, L. Performance improvement of perovskite solar cells through enhanced hole extraction: The Role of Iodide Concentration Gradient. *Sol. Energy Mater. Sol. Cells* **2018**, *185*, 117-123.
20. Zheng, Y.; Kong, J.; Huang, D.; Shi, W.; McMillon-Brown, L.; Katz, H. E.; Yu, J.; Taylor, A. D. Spray Coating of the PCBM Electron Transport Layer Significantly Improves the Efficiency of p-i-n Planar Perovskite Solar Cells. *Nanoscale* **2018**, *10*, 11342-11348.
21. Chen, L.; Wang, G.; Niu, L.; Yao, Y.; Guan, Y.; Cui, Y.; Song, Q. High performance planar p-i-n perovskite solar cells based on a thin Alq₃ cathode buffer layer. *RSC Adv.* **2018**, *8*, 15961-15966.
22. Jun-Yuan, J.; Kuo-Cheng, C.; Tsung-Yu, C.; Pei-Ying, L.; Tzung-Da, T.; Yun-Chorng, C.; Tzung-Fang, G.; Peter, C.; Ten-Chin, W.; Yao-Jane, H. Nickel Oxide Electrode Interlayer in CH₃NH₃PbI₃ Perovskite/PCBM Planar-Heterojunction Hybrid Solar Cells. *Adv. Mater.* **2014**, *26*, 4107-4113.
23. Cui, J.; Meng, F.; Zhang, H.; Cao, K.; Yuan, H.; Cheng, Y.; Huang, F.; Wang, M. CH₃NH₃PbI₃-Based Planar Solar Cells with Magnetron-Sputtered Nickel Oxide. *ACS Appl. Mater. Inter.* **2014**, *6*, 22862-22870.
24. Hu, L.; Peng, J.; Wang, W.; Xia, Z.; Yuan, J.; Lu, J.; Huang, X.; Ma, W.; Song, H.; Chen, W.; Cheng, Y.-B.; Tang, J. Sequential Deposition of CH₃NH₃PbI₃ on Planar NiO Film for Efficient Planar Perovskite Solar Cells. *ACS Photonics* **2014**, *1*, 547-553.
25. Wang, K.-C.; Shen, P.-S.; Li, M.-H.; Chen, S.; Lin, M.-W.; Chen, P.; Guo, T.-F. Low-Temperature Sputtered Nickel Oxide Compact Thin Film as Effective Electron Blocking Layer for Mesoscopic NiO/CH₃NH₃PbI₃ Perovskite Heterojunction Solar Cells. *ACS Appl. Mater. Inter.* **2014**, *6*, 11851-11858.
26. Wang, K.-C.; Jeng, J.-Y.; Shen, P.-S.; Chang, Y.-C.; Diau, E. W.-G.; Tsai, C.-H.; Chao, T.-Y.; Hsu, H.-C.; Lin, P.-Y.; Chen, P.; Guo, T.-F.; Wen, T.-C. p-type Mesoscopic Nickel Oxide/Organometallic Perovskite Heterojunction Solar Cells. *Sci. Rep.* **2014**, *4*, 4756.
27. Zhu, Z.; Bai, Y.; Zhang, T.; Liu, Z.; Long, X.; Wei, Z.; Wang, Z.; Zhang, L.; Wang, J.; Yan, F.; Yang, S. High-Performance Hole-Extraction Layer of Sol-Gel-Processed NiO Nanocrystals for Inverted Planar Perovskite Solar Cells. *Angew. Chem.* **2014**, *126*, 12779-12783.
28. Park Jong, H.; Seo, J.; Park, S.; Shin Seong, S.; Kim Young, C.; Jeon Nam, J.; Shin, H.-W.; Ahn Tae, K.; Noh Jun, H.; Yoon Sung, C.; Hwang Cheol, S.; Seok Sang, I. Efficient CH₃NH₃PbI₃ Perovskite Solar Cells Employing Nanostructured p-Type NiO Electrode Formed by a Pulsed Laser Deposition. *Adv. Mater.* **2015**, *27*, 4013-4019.

29. Zhang, H.; Cheng, J.; Lin, F.; He, H.; Mao, J.; Wong, K. S.; Jen, A. K. Y.; Choy, W. C. H. Pinhole-Free and Surface-Nanostructured NiO_x Film by Room-Temperature Solution Process for High-Performance Flexible Perovskite Solar Cells with Good Stability and Reproducibility. *ACS Nano* **2016**, 10, 1503-1511.
30. Bush, K. A.; Palmstrom, A. F.; Yu, Z. J.; Boccard, M.; Cheacharoen, R.; Mailoa, J. P.; McMeekin, D. P.; Hoye, R. L. Z.; Bailie, C. D.; Leijtens, T.; Peters, I. M.; Minichetti, M. C.; Rolston, N.; Prasanna, R.; Sofia, S.; Harwood, D.; Ma, W.; Moghadam, F.; Snaith, H. J.; Buonassisi, T.; Holman, Z. C.; Bent, S. F.; McGehee, M. D. 23.6%-e=Efficient Monolithic Perovskite/Silicon Tandem Solar Cells with Improved Stability. *Nature Energy* **2017**, 2, 17009.
31. Yin, X.; Chen, P.; Que, M.; Xing, Y.; Que, W.; Niu, C.; Shao, J. Highly Efficient Flexible Perovskite Solar Cells Using Solution-Derived NiO_x Hole Contacts. *ACS Nano* **2016**, 10, 3630-3636.
32. Seo, S.; Park, I. J.; Kim, M.; Lee, S.; Bae, C.; Jung, H. S.; Park, N.-G.; Kim, J. Y.; Shin, H. An Ultra-Thin, un-Doped NiO Hole Transporting Layer of Highly Efficient (16.4%) Organic-Inorganic Hybrid Perovskite Solar Cells. *Nanoscale* **2016**, 8, 11403-11412.
33. You, J.; Meng, L.; Song, T.-B.; Guo, T.-F.; Yang, Y.; Chang, W.-H.; Hong, Z.; Chen, H.; Zhou, H.; Chen, Q.; Liu, Y.; De Marco, N.; Yang, Y. Improved Air Stability of Perovskite Solar Cells via Solution-Processed Metal Oxide Transport Layers. *Nat. Nanotechnol.* **2015**, 11, 75.
34. Guo, Y.; Yin, X.; Liu, J.; Chen, W.; Wen, S.; Que, M.; Tian, Y.; Yang, Y.; Que, W. Effect of the Post-Annealing Temperature on the Thermal-Decomposed NiO_x Hole Contact Layer for Perovskite Solar Cells. *J. Adv. Dielectrics* **2018**, 08, 1850006.
35. Liu, Z.; Zhu, A.; Cai, F.; Tao, L.; Zhou, Y.; Zhao, Z.; Chen, Q.; Cheng, Y.-B.; Zhou, H. Nickel Oxide Nanoparticles for Efficient Hole Transport in p-i-n and n-i-p Perovskite Solar Cells. *J. Mater. Chem. A* **2017**, 5, 6597-6605.
36. Mali, S. S.; Kim, H.; Kim, H. H.; Shim, S. E.; Hong, C. K. Nanoporous p-Type NiO_x Electrode for p-i-n Inverted Perovskite Solar Cell Toward Air Stability. *Mater. Today* **2018**, 483-500.
37. Yongzhen, W.; Fengxian, X.; Han, C.; Xudong, Y.; Huimin, S.; Molang, C.; Zhongmin, Z.; Takeshi, N.; Liyuan, H. Thermally Stable MAPbI₃ Perovskite Solar Cells with Efficiency of 19.19% and Area over 1 cm² achieved by Additive Engineering. *Adv. Mater.* **2017**, 29, 1701073.
38. Mehrdad, N.; Francesco, D. G.; Dong, Z.; Santhosh, S.; Alessia, S.; Wiljan, V.; Afshin, H.; Yulia, G.; Tom, A.; Sjoerd, V.; Ronn, A. Highly Efficient and Stable Flexible Perovskite Solar Cells with Metal Oxides Nanoparticle Charge Extraction Layers. *Small* **2018**, 14, 1702775.
39. Tang, J.; Jiao, D.; Zhang, L.; Zhang, X.; Xu, X.; Yao, C.; Wu, J.; Lan, Z. High-Performance Inverted Planar Perovskite Solar Cells Based on Efficient Hole-Transporting Layers from Well-Crystalline NiO Nanocrystals. *Solar Energy* **2018**, 161, 100-108.
40. Liu, Z.; Chang, J.; Lin, Z.; Zhou, L.; Yang, Z.; Chen, D.; Zhang, C.; Liu, S.; Hao, Y. High-Performance Planar Perovskite Solar Cells Using Low Temperature, Solution-Combustion-Based Nickel Oxide Hole Transporting Layer with Efficiency Exceeding 20%. *Adv. Energ. Mater.* **2018**, 8, 1703432.
41. Zhang, Y.; Yang, M.; Du, J.; Yang, L.; Fan, L.; Liu, X.; Yang, J.; Wang, F. Modulation of Ni³⁺ and Crystallization of Dopant-free NiO_x Hole Transporting Layer for Efficient p-i-n Perovskite Solar Cells. *Electrochim. Acta* **2019**, 319, 41-48.